

Experimental Strategy and Mechanistic View to Boost the Photocatalytic Activity of Cs₃Bi₂Br₉ Lead-Free Perovskite Derivative by g-C₃N₄ Composite Engineering

Lidia Romani, Andrea Speltini, Carlo Nazareno Dibenedetto, Andrea Listorti, Francesco Ambrosio,* Edoardo Mosconi, Angelica Simbula, Michele Saba, Antonella Profumo, Paolo Quadrelli, Filippo De Angelis, and Lorenzo Malavasi*

The rational design of heterojunctions based on metal halide perovskites (MHPs) is an effective route to create novel photocatalysts to run relevant solar-driven reactions. In this work, an experimental and computational study on the synergic coupling between a lead-free Cs₃Bi₂Br₉ perovskite derivative and g-C₃N₄ is presented. A relevant boost of the hydrogen photogeneration by more than one order of magnitude is recorded when going from pure g-C₃N₄ to the Cs₃Bi₂Br₉/g-C₃N₄ system. Effective catalytic activity is also achieved in the degradation of the organic pollutant with methylene blue as a model molecule. Based upon complementary experimental outputs and advanced computational modeling, a rationale is provided to understand the heterojunction functionality as well as the trend of hydrogen production as a function of perovskite loading. This work adds further solid evidence for the possible application of MHPs in photocatalysis, which is emerging as an extremely appealing and promising field of application of these superior semiconductors.

divalent metal cation, and X is a halide anion, have emerged among the most promising materials for optoelectronic applications, because of their tunable direct bandgap, high absorption coefficient, low exciton binding energy, and high carrier mobility.^[1,2] Several potential optoelectronic applications of MHPs have been proposed, spanning from emitters for next-generation light-emitting diodes, emitters in coherent-light sources and mainly as absorbers in solar cells providing high power conversion efficiencies.^[3] Further potential use of MHPs lies in the development of field-effect transistors, photo-detectors, and photo transistors which all require a low exciton binding energy.^[4]

In the last few years, MHPs have also attracted significant attention for their possible use in heterogeneous photocatalysis,

1. Introduction


In the past few years, metal halide perovskites, MHPs, with general formula ABX₃, where A is a monovalent cation, B a

in virtue of the long carrier lifetimes and high mobility, together with a good defect tolerance and easily tunable bandgap in the visible region to catalyze solar-driven reactions.^[5–9] Furthermore, the band alignment of the various MHPs with the most

L. Romani, A. Profumo, P. Quadrelli, L. Malavasi
Department of Chemistry and INSTM
University of Pavia
Via Taramelli 16, Pavia 27100, Italy
E-mail: lorenzo.malavasi@unipv.it

A. Speltini
Department of Drug Sciences
University of Pavia
Via Taramelli 12, Pavia 27100, Italy

C. N. Dibenedetto, A. Listorti
Department of Chemistry
University of Bari "Aldo Moro"
via Orabona 4, Bari 70126, Italy

 The ORCID identification number(s) for the author(s) of this article can be found under <https://doi.org/10.1002/adfm.202104428>.

© 2021 The Authors. Advanced Functional Materials published by Wiley-VCH GmbH. This is an open access article under the terms of the Creative Commons Attribution License, which permits use, distribution and reproduction in any medium, provided the original work is properly cited.

DOI: 10.1002/adfm.202104428

C. N. Dibenedetto
Istituto per i Processi Chimico Fisici del CNR (IPCF-CNR)
c/o Dipartimento di Chimica
Università degli Studi di Bari "Aldo Moro"
via Orabona 4, Bari 70126, Italy

F. Ambrosio, E. Mosconi, F. De Angelis
Computational Laboratory for Hybrid/Organic Photovoltaics (CLHYO)
Istituto CNR di Scienze e Tecnologie Chimiche "Giulio Natta"
(CNR-SCITEC)
Via Elce di Sotto 8, Perugia 06123, Italy
E-mail: francesco.ambrosio@iit.it

F. Ambrosio
Centre for Nano Science and Technology (CNST@PoliMi)
Istituto Italiano di Tecnologia
Milan 20133, Italy

A. Simbula, M. Saba
Dipartimento di Fisica
Università di Cagliari
Monserrato 09042, Italy

F. De Angelis
Department of Chemistry, Biology and Biotechnology
University of Perugia
Via Elce di Sotto 8, Perugia 06123, Italy

common redox half-reactions determines their thermodynamic suitability to effectively run both reduction and oxidation reactions.^[6] Among the solar-driven processes of current interest, MHPs have been studied for the evolution of hydrogen, the reduction of carbon dioxide, the photodegradation of dyes and contaminants, and the synthesis of organic compounds.^[5–9]

MHPs for photocatalytic applications share the same problems of those used as absorbers in photovoltaics (PV): i) the most-efficient MHPs are lead-based with the intrinsic toxicity of this element being extremely undesirable for mass production and ii) the poor stability under moisture/water exposure.^[5] Therefore, the development of novel MHPs for photocatalysis need to overcome these issues. Replacing lead may be achieved by using metals with similar electronic structure and comparable ionic radius to obtain analogous optoelectronic properties along with a stable perovskite structure. Moreover, the organic cations may be replaced with alternative inorganic cations to increase the photostability of the perovskite.^[1]

In this context, given their similar electronic configuration, Group 14 Sn²⁺ and Ge²⁺ and Group 15 Bi³⁺ and Sb³⁺ where employed as Pb²⁺ substitutes to obtain stable perovskite and perovskite-derivate structures.^[1,10] In particular, tin-based perovskites exhibit a narrower bandgap compared with their lead analogues, they have low exciton binding energies and longer carrier diffusion lengths, however they are often sensitive toward moisture and oxygen since Sn²⁺ tends to oxidize to Sn⁴⁺.^[1] Likewise, germanium-based perovskites, while possessing similar electronic conductive behavior, stability and optical properties compared with lead-based perovskites, are also affected by Ge²⁺–Ge⁴⁺ oxidation.^[1] Bi³⁺ has the advantage of having not only an electronic configuration similar to Pb²⁺ but also a comparable ionic radius and, in fact, A₃Bi₂X₉ perovskite-derivates demonstrated high photoluminescence quantum yields (PLQY) and moisture and air stability.^[1,10] On the other hand, antimony-based perovskites, with the same A₃Sb₂X₉ structure of the bismuth-based perovskites, still show low efficiencies.^[1,10]

Given their good water stability, bismuth-based perovskite-derivates have already shown promising results as heterogeneous photocatalysts; Bresolin et al. used Cs₃Bi₂I₉ for the photodegradation of dyes, as model organic pollutants, and for hydrogen evolution.^[11–13] Bhosale et al. employed three different bismuth-based perovskites (Cs₃Bi₂I₉, Rb₃Bi₂I₉, and MA₃Bi₂I₉) for the photoreduction of carbon dioxide to carbon monoxide and methane at the gas–solid interface, while Dai et al. used Cs₃Bi₂Br₉ for the photocatalytic addition of alcohols to epoxides, for the production of β-alkoxyalcohols. Furthermore, they synthesized a heterogeneous structure of Cs₃Bi₂Br₉ nanoparticles embedded in mesoporous silica that they used for the selective photocatalytic activation of C(sp³)–H bonds.^[14–16]

Focusing on the visible-light photogeneration of hydrogen, a few perovskites have already been employed as heterogeneous photocatalysts for the evolution of hydrogen, but, since most perovskites are unstable in aqueous environment, the vast majority of measurements have been conducted in hydrohalic acids that prevent the complete dissolution of the perovskite by common-ion effect.^[5] However, being hydrogen production from concentrated acids hardly sustainable, the development of water-stable photocatalysts is imperative.^[5]

Based on the above considerations, Bi-based perovskite materials are suitable candidates for effective photocatalytic hydrogen evolution in aqueous media due to their demonstrated stability.^[11–13] For this reason, herein, we report the synthesis and the characterization of a new heterogeneous photocatalyst, namely Cs₃Bi₂Br₉/g-C₃N₄, achieved by coupling the semiconducting Cs₃Bi₂Br₉ perovskite derivative (with a bandgap of about 2.7 eV) to the well-known visible-light g-C₃N₄ material (bandgap of about 2.85 eV), that is active under visible light irradiation.^[15] The coupling of MHPs with g-C₃N₄ to create photocatalytically efficient composites is becoming a widespread strategy in the current literature for various kinds of photoreactions.^[17–19] In the present paper, we decided to take advantage of bismuth resistance to oxidation and Cs₃Bi₂Br₉ water stability to develop this new composite material, expecting a positive band-alignment between the two semiconductors and therefore improved charge carrier dynamics as observed by some of us in other composites.^[20,21] The photocatalytic activity of the Cs₃Bi₂Br₉/g-C₃N₄ composites, for different loading amounts of perovskites, has been tested by studying the hydrogen evolution reaction in an aqueous solution as well as the degradation of methylene blue, representative of organic pollutants.^[20,21]

Pristine Cs₃Bi₂Br₉ has been synthesized in dimethylformamide by starting from halide precursors as described in the Experimental Section (see the Experimental Section in the Supporting Information). **Figure 1a** reports the X-ray diffraction (XRD) pattern of as-prepared Cs₃Bi₂Br₉ overlapped to the calculated crystal structure of the expected trigonal symmetry (space group *P-3m*).^[22] In **Figure 1b**, the sketch of the crystal structure is reported, while in **Figure 1c** is shown the appearance of the synthesized yellow powders. As evident from **Figure 1a**, the material is single-phase and presents a slight preferential orientation along the (00*l*) crystal direction. Lattice parameters are *a* = *b* = 8.0526(5) Å and *c* = 9.8460(5) Å. Water stability of Cs₃Bi₂Br₉ has been determined by a leaching test where 15 mg of the perovskite has been placed in 5 mL of water under magnetic stirring, and the amount of Bi in the solution has been determined by inductively coupled plasma-optical emission spectroscopy. At 4, 7, and 16 h of stirring, the Bi amount detected in the solution was always <0.05% (detection limit) of the total amount of bismuth present in the perovskite, indicating an impressive water stability.

As previously mentioned, Cs₃Bi₂Br₉ itself has proven to be a good photocatalytic material under visible-light but, to improve its efficiency, a series of composite materials with g-C₃N₄ at different perovskite loadings (wt%) have been prepared by wet-chemistry as detailed in the Experimental Section (Supporting Information). g-C₃N₄ has been selected by design as a suitable semiconductor to be coupled to Cs₃Bi₂Br₉ in virtue of their relative bandgaps being around ≈2.7 eV for Cs₃Bi₂Br₉ and ≈2.85 eV for g-C₃N₄. Therefore, we expected a favorable band-alignment between the two semiconductors thus favoring charge transfer and reducing the charge recombination, as previously observed for a (CH₃)₂NH₂SnBr₃/g-C₃N₄ composite.^[15,16,21]

The Cs₃Bi₂Br₉/g-C₃N₄ composites (wt% of perovskite: 1, 2.5, 3.5, 5, 10, and 15) have been characterized in terms of crystal structure, optical properties, and morphology. **Figure 2a** shows the XRD patterns of all prepared materials starting from pure g-C₃N₄ (bottom of the figure, blue pattern) followed by

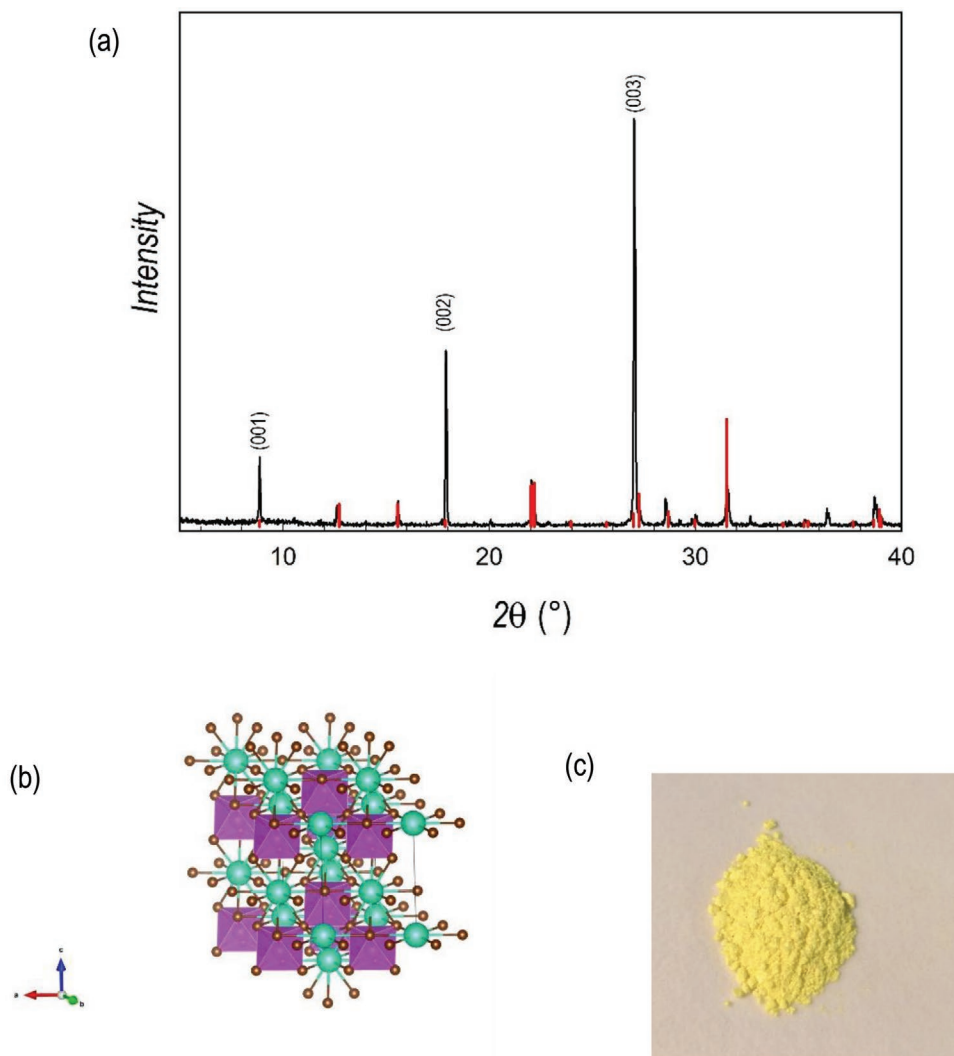


Figure 1. a) XRD pattern of $\text{Cs}_3\text{Bi}_2\text{Br}_9$ synthesized by wet-chemistry where red vertical bars refer to the reflection positions for trigonal structure of the perovskite ($P-3m$); b) sketch of the crystal structure and c) appearance of the bulk sample.

composites at increasing amounts of $\text{Cs}_3\text{Bi}_2\text{Br}_9$ (pattern of pure $\text{Cs}_3\text{Bi}_2\text{Br}_9$ is reported in the top of the figure, in red).

Pure $\text{g-C}_3\text{N}_4$ shows the common diffraction pattern mainly characterized by a typical broad peak around 28° (vertical dotted blue line) which is found in all the composites, where carbon nitride represents the main phase. Concerning the $\text{Cs}_3\text{Bi}_2\text{Br}_9$ contribution to the patterns, this starts to be slightly visible already at 2.5% of loading, but its clear signature is found starting from about 5% (see vertical dotted red lines), with a progressive relative intensity increase which follows the addition of the perovskite.

The optical properties of the $\text{Cs}_3\text{Bi}_2\text{Br}_9/\text{g-C}_3\text{N}_4$ composites have been determined by UV–VIS absorption spectroscopy and the data are reported in Figure 2b as a function of energy. Pure $\text{g-C}_3\text{N}_4$, and composites with 1% and 2.5% loading of perovskite, have very similar absorption spectra, while a contribution shifting to lower-energies starts to be evident from the 3.5% sample and becomes clearer when increasing the perovskite amount and can be associated with the $\text{Cs}_3\text{Bi}_2\text{Br}_9$ exciton, as

previously reported for this and other layered $\text{Cs}_3\text{Bi}_2\text{X}_9$ perovskites.^[5,23,24] The normalized photoluminescence spectra of pure compounds and composites, reported in Figure 2c, present a similar threshold behavior. Pure $\text{g-C}_3\text{N}_4$, shows a relatively broad emission, peaking at 2.7 eV, corresponding to the band–band PL phenomenon of $\text{g-C}_3\text{N}_4$, only 0.15 eV downshifted relatively to its bandgap energy (Figure 2c).^[25] Noticeably, the composites up to 3.5% loading of perovskite, show very similar emission spectra while, starting from the 5% sample, a shift toward low energies is observed. This suggests that the emission begins to be affected by contributions from $\text{Cs}_3\text{Bi}_2\text{Br}_9$ at higher loading of the perovskite. In fact, pristine $\text{Cs}_3\text{Bi}_2\text{Br}_9$ shows a relatively narrow and weak emission peaking at 2.59 eV and, although with a broader energy distribution, the emission of the 10% composite resembles it.

The morphologies of the pure samples and composites have been assessed by scanning electron microscopy (SEM) and are reported in Figure S1 (Supporting Information). Surface area of all the samples has been determined by B.E.T method and

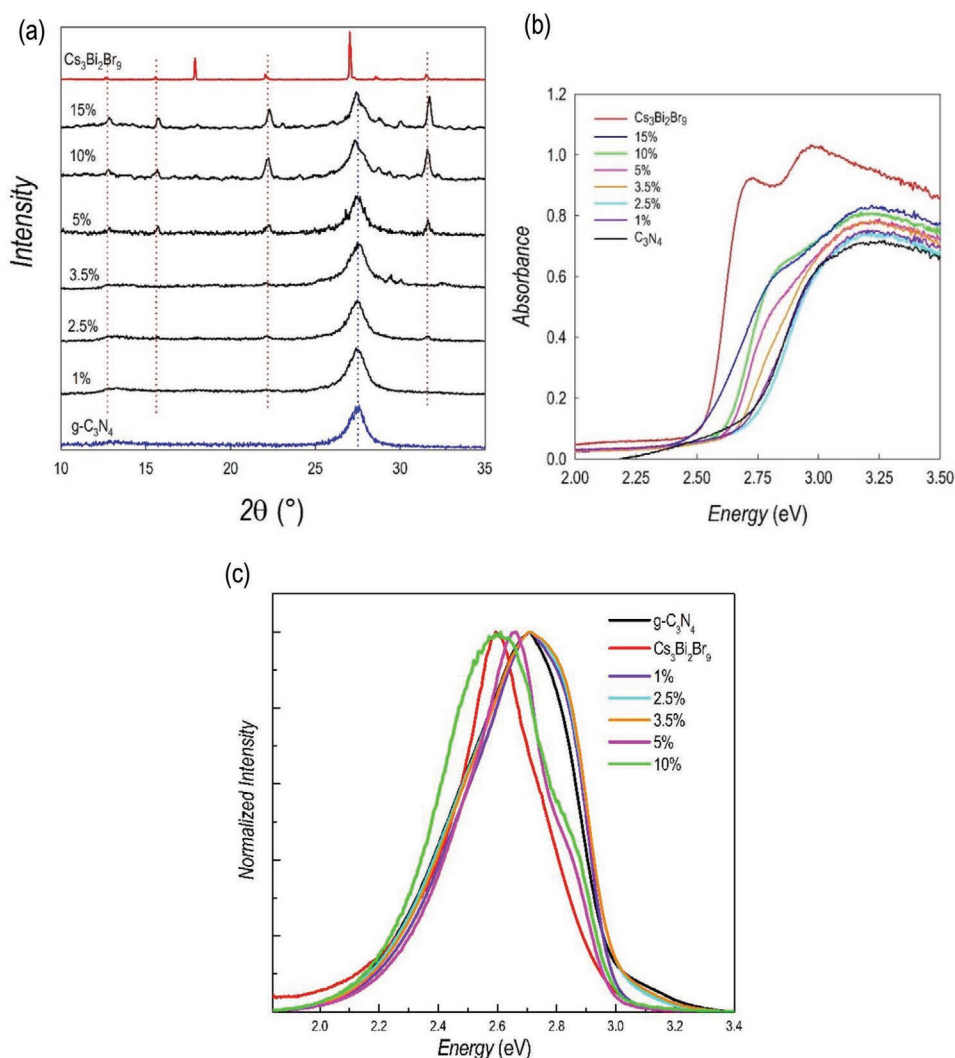


Figure 2. a) XRD pattern of Cs₃Bi₂Br₉/g-C₃N₄ composites at different percentages of perovskite loading (wt%). g-C₃N₄ and Cs₃Bi₂Br₉ refer to pristine materials. b) Absorption spectra of the composites versus energy (percentages refers to the wt% of Cs₃Bi₂Br₉ in the composite); c) Emission spectra of Cs₃Bi₂Br₉/g-C₃N₄ composites powders at different percentages of perovskite loading (wt%). g-C₃N₄ and Cs₃Bi₂Br₉ refer to pristine materials. $\lambda_{\text{ex}} = 375$ nm.

the results are reported in Table S1 in the Supporting Information. As-prepared g-C₃N₄ shows a surface area around 76 m² g⁻¹ which remains substantially unchanged, within the estimated standard deviation of the measurement, up to 5% loading of perovskite. A slight reduction of surface area is observed at 10% and 15% loadings reaching a value around 50 m² g⁻¹. In general, however, the variation in the surface area is not particularly large thus indicating, with reference to the photocatalytic results which will be shown later, that this is not the key parameter in affecting the trend of composites activity.

The solar-driven catalytic efficiency of the prepared composites has been first determined in terms of hydrogen evolution rate (HER) by employing usual protocols applied in the current literature for g-C₃N₄-based composites, i.e., in 10% v/v aqueous triethanolamine (TEOA), as a typical sacrificial agent, and with Pt (3 wt%) as metal cocatalyst.^[26] The results reported in the following have been performed on several sample replicas, and the experimental details of the hydrogen evolution tests are

reported in the Experimental Section. The HERs results as a function of perovskite loading for pure g-C₃N₄ and for the composites are shown in **Figure 3a**.

Figure 3a clearly shows an impressive enhancement of the HER from pure g-C₃N₄ (81 $\mu\text{mol g}^{-1} \text{h}^{-1}$) to 1% and 2.5% Cs₃Bi₂Br₉/g-C₃N₄ composites, reaching, at this last perovskite loading, the highest HER of about $\approx 1050 \mu\text{mol g}^{-1} \text{h}^{-1}$. Further perovskite loading leads to a progressive reduction of the efficiency of hydrogen photogeneration, and this trend has been later analyzed by coupling advanced optical characterization tools and computational modeling. Clearly, achieving an optimal HER at a low-doping of perovskite cocatalyst is a positive result in terms of material manufacturing and cost. Let us highlight that pure Cs₃Bi₂Br₉, under the same experimental conditions used for the composites, evolves only $\approx 22 \mu\text{mol g}^{-1} \text{h}^{-1}$ of hydrogen. This result, coupled to the HER of pure carbon nitride (81 $\mu\text{mol g}^{-1} \text{h}^{-1}$), clearly indicates a strong and effective synergy between the two semiconductors

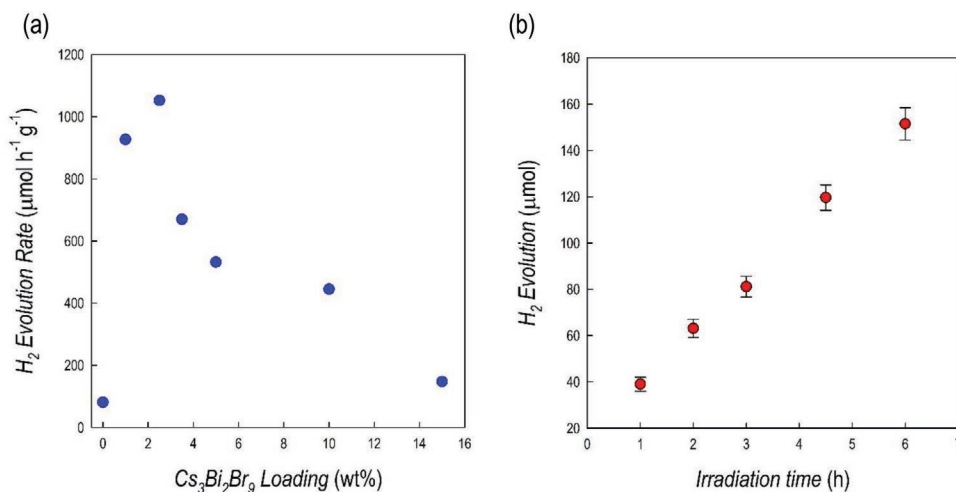


Figure 3. a) Hydrogen evolution rates for Cs₃Bi₂Br₉/g-C₃N₄ composites (1 g L⁻¹) at different percentages of MHP loading in 10% v/v TEOA aqueous solution with Pt 3wt%, under simulated solar light (6 h irradiation, Xenon lamp, 500 W m⁻², 300–800 nm, IR-treated soda lime glass UV outdoor filter). RSD < 10% (*n* = 3); b) Hydrogen evolution profile over irradiation time for the 2.5 wt% Cs₃Bi₂Br₉/g-C₃N₄ composite (1 g L⁻¹, 10% v/v TEOA, 3 wt% Pt), under simulated solar light (Xenon lamp, 500 W m⁻², 300–800 nm, IR-treated soda lime glass UV outdoor filter). RSD < 10% (*n* = 3).

in the Cs₃Bi₂Br₉/g-C₃N₄ composites. The origin of such effect will be further addressed later in the paper. For the optimal composite, namely at 2.5 wt% of Cs₃Bi₂Br₉, the kinetics of H₂ was studied and the trend, reported in Figure 3b, indicates a substantial linear increase of the hydrogen production as function of time. The XRD pattern of the spent catalyst has been collected and compared to the fresh material. This has been done in particular for the sample with 15% of Cs₃Bi₂Br₉, to better highlight the perovskite reflections. The comparison of the two patterns is reported in Figure S2 (Supporting Information) indicating a very good stability of the material after a photocatalytic run. In addition, on the best performing composite, namely 2.5 wt% Cs₃Bi₂Br₉/g-C₃N₄, we carried out four successive photocatalytic runs by collecting the sample each time by centrifugation (see the Experimental Details). The performance of the HER in this reuse test is reported in Figure S3 (Supporting Information). This last test revealed, overall, a good stability of the composite over 4 cycles, although with a drop in efficiency after the first cycle of about 40%. After the first cycle the HER remains constant indicating a very effective synergy between the two semiconductors in the composite, still 8 times more efficient than pristine g-C₃N₄.

Finally, the photocatalytic activity of the best performing composite (2.5 wt% Cs₃Bi₂Br₉/g-C₃N₄) was also tested to verify its ability toward the decomposition of organic dyes, by selecting methylene blue (MB) as a representative model compound of this class. The results of the test are reported in Figure 4 showing the time-dependent absorbance for pure g-C₃N₄, for the composite, and for direct photolysis (see details in the Supporting Information). This experiment confirms the very good performance of the Cs₃Bi₂Br₉/g-C₃N₄ composite also for the organic dye degradation, with a total degradation achieved in 60 min. Pure g-C₃N₄ is not able to fully degrade MB even after 90 min of irradiation (total time of the experiment).

To deepen the rational upon composite behavior and the peculiar effect of perovskite inclusion we prepared a series thin films deposited on transparent glass support. To do so,

we dispersed the composites and the reference compounds in a Nafion matrix. Their normalized photoluminescence spectra are reported in Figure S4 (Supporting Information). These emissions are dominated by the broad and intense features of graphitic carbon nitride. These broadbands, that completely cover the weak perovskite emission (Figure S5, Supporting Information), derive from the superimposition of multiple electronic transitions (Figure S6, Supporting Information).^[27] Apart from the high energy one, which is a direct consequence of the absorption, and it is usually centered at around 440 nm (P1), the

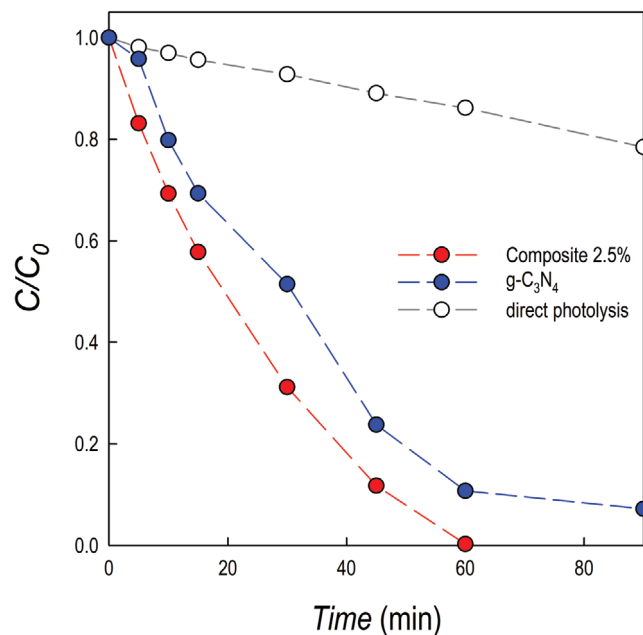


Figure 4. Variation of MB concentration as a function of irradiation time for Cs₃Bi₂Br₉/g-C₃N₄ composite at 2.5 wt% loading (red dots) and g-C₃N₄ (blue dots), compared to photolysis effect (empty dots); conditions: 1 g L⁻¹ catalyst, 250 W m⁻² simulated solar light.

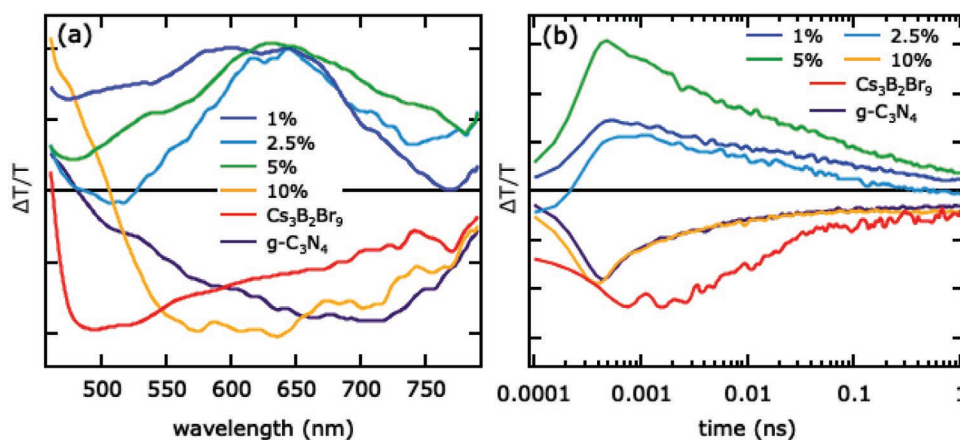


Figure 5. Transient absorption spectroscopy of $\text{Cs}_3\text{Bi}_2\text{Br}_9/\text{g-C}_3\text{N}_4$ composites thin films at different percentages of perovskite loading (wt%). $\text{g-C}_3\text{N}_4$ and $\text{Cs}_3\text{Bi}_2\text{Br}_9$ refer to pristine materials. a) TAS spectrum, integrated in time. b) Time decay of spectrally integrated TAS signals as a function of the pump-probe time delay (note the logarithmic time scale). $\lambda_{\text{ex}} = 345$ nm.

low energy features at 455 nm (P2) and 505 nm (P3) are favored by a nonradiative population of subband states, their intensity depends in fact on the population of a sp^2 C–N π band which is boosted by the presence of defects in the material.^[27]

By zooming the emission band peak, inset of Figure S4 (Supporting Information), it is clear how for the initial perovskite inclusion (1 wt% sample) there is a reduction of low energy bands emission, P2 and P3, respectively, in other words a reduction of the defects mediated radiative paths. Conversely, by increasing the perovskite content, the low energy transition becomes more and more pronounced. Noticeably, it has been proposed that the photocatalytic activity of $\text{g-C}_3\text{N}_4$ could be related to the material purity. Samples containing large defect densities were less efficient in degrading organic pollutant under light irradiation, and the evidence coming from steady state PL shows how perovskite inclusion can improve $\text{g-C}_3\text{N}_4$ purity to a certain level while, when the doping is greater than 2.5 wt% this inclusion starts to be detrimental resulting in nonradiative paths becoming more and more active.^[28] Clearly, $\text{Cs}_3\text{Bi}_2\text{Br}_9$, in addition to defect distribution influence, also acts as an active player in the charge dynamics fate in virtue of its accessible states.

Herein a powerful technique to understand the excited state dynamics in photocatalytic materials is femtosecond transient absorption spectroscopy (TAS), a pump-probe technique consisting in measuring the ultrafast transient absorption changes induced by pulsed laser excitation. Thin films of pure $\text{g-C}_3\text{N}_4$ and composites were excited with 100 fs, 345 nm, laser pulses from a KHz regenerative amplifier seed an optical parametric oscillator to create photoexcitations (Coherent Libra and Light Conversion Topas 800, respectively). Absorption changes were monitored with a broadband, white light supercontinuum probe, generated by focusing the regenerative amplifier fundamental output (800 nm) onto a sapphire plate and detected by fiber-coupled, complementary metal-oxide-semiconductor grating spectrometers (Ultrafast Systems Helios). TAS is a complementary technique with respect to time-resolved photoluminescence because it is sensitive to all photoexcitations, even the dark ones, like charge-separated states that are crucial to achieve photocatalytic activity. Despite similar PL dynamics, composites

with different perovskite fractions displayed extremely different TAS signals (see Figure 5). For both starting materials, $\text{g-C}_3\text{N}_4$ and $\text{Cs}_3\text{Bi}_2\text{Br}_9$, as well as composites with 10 wt% perovskite loading, a broadband, negative differential transmission signal is observed, corresponding to photoinduced absorption. On the contrary, composites with perovskite loading fractions of 1, 2.5, and 5 wt%, i.e., the composites with enhanced photocatalytic activity, a positive differential transmission signal appears, corresponding to bleaching (see Figure 5b). Photoinduced absorption in $\text{g-C}_3\text{N}_4$ has been attributed to photoexcited electrons.^[29–33] Concerning the pure perovskite, a broadband photoinduced absorption below the bandgap has been associated in double halide perovskites with Cs and Bi to self-trapped excitons, meaning optical excitations stabilized by a lattice relaxation.^[24] In contrast, bleaching, due to phase-space filling in the excited state, only occurs at photon energies corresponding to the bandgap, i.e., at the high-energy boundary of the spectral region we investigated.^[34] On the other hand, bleaching is not expected as an intrinsic effect for photon energies below the bandgap, and therefore could be attributed to the filling of defect states, most probably at the interface separating the two materials. TAS measurements therefore point to the fact that the addition of $\text{Cs}_3\text{Bi}_2\text{Br}_9$ to $\text{g-C}_3\text{N}_4$, at least for loading fractions lower than 5%, introduces a path for optical excitations that does not exist in pure materials. For perovskite loading fractions more than 5 wt%, such an effect seems to fade, as the TAS signal reverts to both a spectral shape and a time decay similar to pure $\text{g-C}_3\text{N}_4$.

The origin of this peculiar optical behavior at the bases of the superior performances of the $\text{Cs}_3\text{Bi}_2\text{Br}_9/\text{g-C}_3\text{N}_4$ composites has been further investigated by advanced first-principles calculations (see the Supporting Information). We align the band edges of $\text{g-C}_3\text{N}_4$ and $\text{Cs}_3\text{Bi}_2\text{Br}_9$ with respect to a computational standard hydrogen electrode via the vacuum level. For both materials, the calculations are carried out in order to reproduce the measured fundamental gaps (cf. Supporting Information).^[34–36] The results illustrated in Figure 6 show that the alignment of the band edges between the constituents of the composite should in principle favor efficient charge separation. In fact, the valence and conduction band edges of $\text{g-C}_3\text{N}_4$ ($\text{Cs}_3\text{Bi}_2\text{Br}_9$) are placed at 6.0 (5.79) and 3.00 (2.79) eV below the

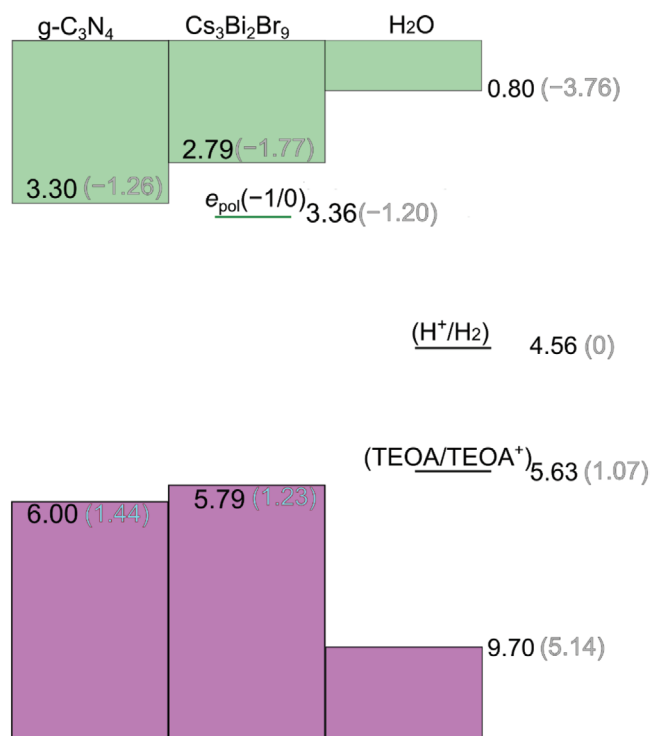


Figure 6. Valence band (VB) and conduction band (CB) edges of g-C₃N₄ and Cs₃Bi₂Br₉ aligned with the band edges of liquid water and with the H⁺/H₂ and TEOA/TEOA⁺ redox level (cf. ref. [5]) through the vacuum level. The (-1/0) charge transition level of the electron polaron calculated for Cs₃Bi₂Br₉ is also reported. Values are referred to the vacuum level (black) and to the standard hydrogen electrode (SHE, gray) using the computational alignment achieved in ref. (4). All values are given in eV.

vacuum level, respectively. Therefore, photogenerated holes in the valence band (VB) of g-C₃N₄ may migrate to that of Cs₃Bi₂Br₉ while, in turn, photoexcited electrons in Cs₃Bi₂Br₉ are easily transferred to the conduction band (CB) of g-C₃N₄. The efficient separation and transport of photoinduced electrons and holes induced by such a favorable alignment of energy levels may curb bimolecular recombination of the charge carriers, thus enhancing the photocatalytic activity of the composite with respect to the separated materials. Nevertheless, we underline that the values reported in Figure 6 refer to the fundamental bandgap of both materials. However, Cs₃Bi₂Br₉ shows a sizable exciton (cf. Figure 2b and ref. [24]) and, for this reason, photogenerated carriers within the perovskite might remain self-trapped and, therefore, not easily transferred across the composite. Further hints suggesting this kind of behavior are given by the emission spectra for which we observe, at higher loading of the perovskite, changes in the spectrum which are associated to the perovskite contribution. However, the peak at 2.59 eV for Cs₃Bi₂Br₉ is clearly different from the 2.85 eV value that should be expected from the fundamental bandgap of the material, thus indicating that emission is occurring from a localized in-gap state.

Therefore, the calculated band alignment does not explain the bizarre trend in hydrogen evolution rates as a function of the different Cs₃Bi₂Br₉ loading in the composite (cf. Figure 3), nor the shift observed in the absorption and in the emission

spectra upon composite loading. To solve this conundrum, we investigate the possible occurrence of hole and electron polarons by combining electronic structure calculations with a grand-canonical formulation of defect in semiconductors (see Supporting Information). In fact, the Cs₃Bi₂Br₉ exciton might evolve into separate small hole and electron polarons (i.e., self-trapped excitons), as previously observed for both Bi-based semiconductors and layered perovskites.^[24,37–40] For instance, localization of photogenerated holes onto a bromide dimer (so-called V-center defect typical of metal halides) has been suggested by a recent study.^[41–43]

We first investigate hole polaron formation and we verify that self-hole trapping on a Bi-bridging Br₂⁻ dimer should be ruled out as it is energetically unfavored (see the Supporting Information). Therefore, the hole transfer across the composite is favorable (cf. Figure 6) and no trapping in the perovskite is envisaged, thus ensuring that charge losses are avoided. In stark contrast, upon injection of a single electron in bulk Cs₃Bi₂Br₉, we observe strong localization of the charge around a Bi atom, i.e., self-electron trapping, which is associated with a sizable rearrangement of the local structure as shown in Figure 7. In the charged system, the electron is found to localize upon distortion of a BiBr₆³⁻ subunit: in particular, the distortion brings a substantial increase (from 2.98 to 3.51 Å, cf. Figure 7) in the Bi–Br bond length for the Br atom bridging two adjacent BiBr₆³⁻.

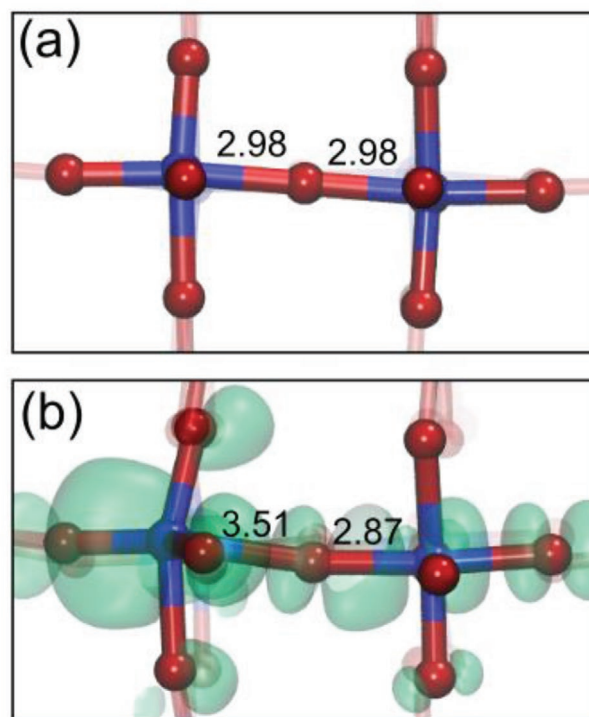


Figure 7. Stick&ball representation of a) neutral bulk Cs₃Bi₂Br₉ and b) Cs₃Bi₂Br₉ bearing an electron polaron (cf. main text). Bi atoms are given in blue and Br in red. Cs atoms are not included for ease of visualization. Isodensity representation of the electron is given in green. The z axis lies vertically. For comparison, we provide the lengths (Å) of the Bi–Br bonds changed upon polaron formation.

binding energy (see Supporting Information) of 0.59 eV for this polaronic state, thus further demonstrating that the small polaron may act as a deep trap in the gap of Cs₃Bi₂Br₉. The associated (−1/0) charge transition level (cf. Figure 6) is found to lie 3.36 eV below the vacuum level and entails an energy gap of 2.43 eV, which is consistent with the low-energy emission measured for the perovskite and for the composites at high % loading.

Overall, self-trapping of the photogenerated electrons can explain the unsatisfactory performances of composites featuring a perovskite loading >5%, for which we observe a very limited enhancement of the hydrogen production with respect to the separated materials. In this sense, we also note that, TAS measurements, which indicate a broadband photoinduced absorption for the perovskite, typically associated with self-trapped excitons, are consistent with the proposed physical picture, resulting in the loss of any synergistic enhancement of hydrogen production. At variance with this, the absence of any spectroscopic signature of Cs₃Bi₂Br₉ for low-loading composites coupled with the high hydrogen yield, suggests that charge trapping in the perovskite might be avoided in this case. Since photoexcitation of Cs₃Bi₂Br₉ could not result in electron transfer from its fundamental CB to that of g-C₃N₄ because of the strong exciton, a possible direct excitation mechanism, e.g., from VB to g-C₃N₄ CB may be operative for small Cs₃Bi₂Br₉ particles dispersed on the g-C₃N₄ surface or among its layers, thus bypassing charge localization, in line with what has been previously observed in dye-sensitized solar cells or in plasmonic photocatalytic composites.^[43,44] In this case, TAS measurements also suggest the possible occurrence of new localized in-gap states at the complex Cs₃Bi₂Br₉/g-C₃N₄ interface, that may act as catalytic sites, thus further motivating the observed boost in hydrogen production.

2. Conclusions

In the present paper, we reported the design of catalytically active composites based on the coupling between Cs₃Bi₂Br₉ and g-C₃N₄ to create a heterojunction where the energy levels alignment between the two semiconductors provides an effective improvement of photoactivity. The samples have been tested for the hydrogen evolution reaction and organic dye degradation identifying the optimal amount of Cs₃Bi₂Br₉ in the composite, namely 2.5 wt%. The synergistic effect allows an impressive increase of photogenerated H₂ from about 81 μmol g^{−1} h^{−1} of pure g-C₃N₄ to ≈1050 μmol g^{−1} h^{−1} for the 2.5 wt% Cs₃Bi₂Br₉/g-C₃N₄ composite. The latter resulted also to be significantly more active in methylene blue degradation with respect to pure carbon nitride. Steady state and ultrafast transient spectroscopic investigations suggest a peculiar charge dynamics in these systems influenced by the perovskite loading. Low levels of perovskite inclusion act both on curing g-C₃N₄ material defects than on funneling the charges upon localized states. Those active sites could be fundamental in boosting the photocatalytic performances of low loading composites. Advanced computational modeling further adds to the rationale behind the microscopic mechanism favoring an efficient charge separation in the composite and, in addition, provides a clue to understand

the optical investigation outputs and the trend of HER as a function of perovskite amount. To conclude, this work further consolidates the actual route toward the application of lead-free MHPs as active photocatalytic materials taking advantage of a rationale design of effective heterojunctions.

Supporting Information

Supporting Information is available from the Wiley Online Library or from the author.

Acknowledgements

F.A., E.M., and F.D.A. acknowledge support from the Ministero Istruzione dell'Università e della Ricerca (MIUR) and the University of Perugia through the program "Dipartimenti di Eccellenza 2018–2022" (grant AMIS) and from the European Union's Horizon 2020 research and innovation programme under Grant Agreement No. 764047 of the Espresso project." L.M. acknowledges financial support from R.S.E. SpA (Ricerca sul Sistema Energetico).

Conflict of Interest

The authors declare no conflict of interest.

Data Availability Statement

Research data are not shared.

Keywords

computational modellings, hydrogen photogenerations, lead-free perovskites, metal halide perovskites, photocatalysts

Received: May 11, 2021
Revised: August 5, 2021
Published online: September 6, 2021

- [1] X. Wang, T. Zhang, Y. Lou, Y. Zhao, *Mater. Chem. Front.* **2019**, *3*, 365.
- [2] S. D. Stranks, H. J. Snaith, *Nat. Nanotechnol.* **2015**, *10*, 391.
- [3] Y. Li, X. Zhang, H. Huang, S. V. Kershaw, A. L. Rogach, *Mater. Today* **2020**, *32*, 204.
- [4] Y. Fu, H. Zhu, J. Chen, M. P. Hautzinger, X.-Y. Zhu, S. Jin, *Nat. Rev. Mater.* **2019**, *4*, 169.
- [5] L. Romani, L. Malavasi, *ACS Omega* **2020**, *5*, 25511.
- [6] H. Huang, B. Pradhan, J. Hofkens, M. B. J. Roeffaers, J. A. Steele, *ACS Energy Lett.* **2020**, *5*, 1107.
- [7] V. Armenise, S. Colella, F. Fracassi, A. Listorti, *Nanomaterials* **2021**, *11*, 433.
- [8] K. A. Huynh, D. L. T. Nguyen, V.-H. Nguyen, D.-V. N. Vo, Q. T. Trinh, T. P. Nguyen, S. Y. Kim, Q. V. Le, *J. Chem. Technol. Biotechnol.* **2020**, *95*, 2579.
- [9] B.-M. Bresolin, Y. Park, D. W. Bahnemann, *Catalysts* **2020**, *10*, 709.
- [10] Z. Jin, Z. Zhang, J. Xiu, H. Song, T. Gatti, Z. He, *J. Mater. Chem. A* **2020**, *8*, 16166.

- [11] B.-M. Bresolin, C. Günemann, D. W. Bahnemann, M. Sillanpää, *Nanomaterials* **2020**, *10*, 763.
- [12] B.-M. Bresolin, P. Sgarbossa, D. W. Bahnemann, M. Sillanpää, *Sep. Purif. Technol.* **2020**, *251*, 117320.
- [13] B.-M. Bresolin, N. O. Balayeva, L. I. Granone, R. Dillert, D. W. Bahnemann, M. Sillanpää, *Sol. Energy Mater. Sol. Cells* **2020**, *204*, 110214.
- [14] S. S. Bhosale, A. K. Kharade, E. Jokar, A. Fathi, S. Chang, E. W.-G. Diau, *J. Am. Chem. Soc.* **2019**, *141*, 20434.
- [15] Y. Dai, H. Tüysüz, *ChemSusChem* **2019**, *12*, 2587.
- [16] Y. Dai, C. Poidevin, C. Ochoa-Hernández, A. A. Auer, H. Tüysüz, *Angew. Chem., Int. Ed.* **2020**, *59*, 5788.
- [17] R. Cheng, H. Jin, M. B. J. Roeflaers, J. Hofkens, E. Debroye, *ACS Omega* **2020**, *5*, 24495.
- [18] M. Corti, R. Chiara, L. Romani, B. Mannucci, L. Malavasi, P. Quadrelli, *Catal. Sci. Technol.* **2021**, *11*, 2292.
- [19] M. Zhang, W. Wang, F. Gao, D. Luo, *Catalysts* **2021**, *11*, 505.
- [20] L. Romani, A. Bala, V. Kumar, A. Speltini, A. Milella, F. Fracassi, A. Listorti, A. Profumo, L. Malavasi, *J. Mater. Chem. C* **2020**, *8*, 9189.
- [21] L. Romani, A. Speltini, F. Ambrosio, E. Mosconi, A. Profumo, M. Marelli, S. Margadonna, A. Milella, F. Fracassi, A. Listorti, F. De Angelis, L. Malavasi, *Angew. Chem., Int. Ed.* **2021**, *60*, 3611.
- [22] F. Lazarini, *Acta Crystallogr. B* **1977**, *33*, 2961.
- [23] K. K. Bass, L. Estergreen, C. N. Savory, J. Buckeridge, D. O. Scanlon, P. I. Djurovich, S. E. Bradforth, M. E. Thompson, B. C. Melot, *Inorg. Chem.* **2017**, *56*, 42.
- [24] K. M. McCall, C. C. Stoumpos, S. S. Kostina, M. G. Kanatzidis, B. W. Wessels, *Chem. Mater.* **2017**, *29*, 4129.
- [25] K. He, J. Xie, Z.-Q. Liu, N. Li, X. Chen, J. Hu, X. Li, *J. Mater. Chem. A* **2018**, *6*, 13110.
- [26] S. Cao, J. Low, J. Yu, M. Jaroniec, *Adv. Mater.* **2015**, *27*, 2150.
- [27] A. Sharma, M. Varshney, K. H. Chae, S. O. Won, *Curr. Appl. Phys.* **2018**, *18*, 1458.
- [28] Y. Yuan, L. Zhang, J. Xing, M. I. B. Utama, X. Lu, K. Du, Y. Li, X. Hu, S. Wang, A. Genç, R. Dunin-Borkowski, J. Arbiol, Q. Xiong, *Nanoscale* **2015**, *7*, 12343.
- [29] R. Godin, Y. Wang, M. A. Zwijnenburg, J. Tang, J. R. Durrant, *J. Am. Chem. Soc.* **2017**, *139*, 5216.
- [30] H. Kasap, C. A. Caputo, B. C. M. Martindale, R. Godin, V. W. Lau, B. V. Lotsch, J. R. Durrant, E. Reisner, *J. Am. Chem. Soc.* **2016**, *138*, 9183.
- [31] H. Zhang, Y. Chen, R. Lu, R. Li, A. Yu, *Phys. Chem. Chem. Phys.* **2016**, *18*, 14904.
- [32] C. Ye, J.-X. Li, Z.-J. Li, X.-B. Li, X.-B. Fan, L.-P. Zhang, B. Chen, C.-H. Tung, L.-Z. Wu, *ACS Catal.* **2015**, *5*, 6973.
- [33] W. Yang, R. Godin, H. Kasap, B. Moss, Y. Dong, S. A. J. Hillman, L. Steier, E. Reisner, J. R. Durrant, *J. Am. Chem. Soc.* **2019**, *141*, 11219.
- [34] J. Luo, X. Wang, S. Li, J. Liu, Y. Guo, G. Niu, L. Yao, Y. Fu, L. Gao, Q. Dong, C. Zhao, M. Leng, F. Ma, W. Liang, L. Wang, S. Jin, J. Han, L. Zhang, J. Etheridge, J. Wang, Y. Yan, E. H. Sargent, J. Tang, *Nature* **2018**, *563*, 541.
- [35] Z. Guo, F. Ambrosio, W. Chen, P. Gono, A. Pasquarello, *Chem. Mater.* **2018**, *30*, 94.
- [36] F. Ambrosio, G. Miceli, A. Pasquarello, *J. Chem. Phys.* **2015**, *143*, 244508.
- [37] F. Ambrosio, Z. Guo, A. Pasquarello, *J. Phys. Chem. Lett.* **2018**, *9*, 3212.
- [38] J. Wiktor, I. Reshetnyak, F. Ambrosio, A. Pasquarello, *Phys. Rev. Mater.* **2017**, *1*, 022401.
- [39] J. Wiktor, F. Ambrosio, A. Pasquarello, *ACS Energy Lett.* **2018**, *3*, 1693.
- [40] D. B. Mitzi, K. Chondroudis, C. R. Kagan, *Inorg. Chem.* **1999**, *38*, 6246.
- [41] Z. Cheng, J. Lin, *CrystEngComm* **2010**, *12*, 2646.
- [42] C. Liu, Y. Wang, H. Geng, T. Zhu, E. Ertekin, D. Gosztola, S. Yang, J. Huang, B. Yang, K. Han, S. E. Canton, Q. Kong, K. Zheng, X. Zhang, *J. Am. Chem. Soc.* **2019**, *141*, 13074.
- [43] A. I. Popov, E. A. Kotomin, J. Maier, *Solid State Ionics* **2017**, *302*, 3.
- [44] F. D. Angelis, *Chem. Phys. Lett.* **2010**, *493*, 323.
- [45] C. Boerigter, R. Campana, M. Morabito, S. Linic, *Nat. Commun.* **2016**, *7*, 10545.